Numerical simulation of LNG tanks exposed to fire

Numerical simulation of LNG tanks exposed to fire

Revised Version

Tommaso IANNACCONE[a], Giordano Emrys SCARPONI[a], Gabriele LANDUCCI[b], Valerio COZZANI[a,*]

[a] Laboratory of Industrial Safety and Environmental Sustainability - Department of Civil, Chemical, Environmental and Material Engineering, Alma Mater Studiorum – University of Bologna, via Terracini 28, 40131, Bologna, Italy

[b] Department of Civil and Industrial Engineering, University of Pisa, Largo Lucio Lazzarino 2, 56126, Pisa (Italy)

(*) Author to whom correspondence should be addressed.
tel. (+39)-051-2090240; fax (+39)-051-2090247
e-mail: valerio.cozzani@unibo.it

Submitted for publication in:

Process Safety and Environmental Protection

Abstract

The increasing use of Liquefied Natural Gas (LNG) as a fuel for ships and vehicles poses relevant safety concerns, extended to the entire LNG supply chain and distribution network. Understanding the phenomena associated with the behavior of LNG tanks exposed to severe heat sources is thus a fundamental issue to identify potential safety-critical scenarios. The experimental data and modeling approaches currently available, mainly referring to small-scale pilot vessels, feature relevant limitations when extended to large-scale applications. In the present study, a two-dimensional non-equilibrium computational fluid dynamics model (2D CFD) of LNG tanks exposed to fire engulfing scenarios was developed. The 2D CFD model was validated against experimental bonfire data and was extended to simulate the behavior of large-scale vessels used in specific industrial applications, as the road transportation of LNG and the fuel supply of ships. A set of Key Performance Indicators (KPIs) was defined to support the safety assessment of LNG tanks, and to identify the potential transition to safety critical regions during fire exposure. The CFD results obtained allowed investigating the influence of operative parameters and geometry on the pressure build-up in the tanks, as well as on the transient evolution of complicating phenomena, such as the thermal stratification. The KPIs defined provide a useful support for the design of safety systems and for decision making in emergency response.

Keywords

CFD Modelling; LNG; Cryogenic tanks; Pressurization rate; Temperature stratification; Safety assessment; Emergency response

List of abbreviations

ADR	European Agreement Concerning the International Carriage of Dangerous Goods by Road	LPG	Liquefied Petroleum Gas
BLEVE	Boiling Liquid Expanding Vapor Explosion	MAWP	Maximum Allowed Working Pressure
BOG	Boil Off Gas	MDT	Maximum Design Temperature
CFD	Computational Fluid Dynamics	NIST	National Institute of Standards and Technology
EI	Energy Index	PI	Pressure Index
IGF	International Code of Safety for Ships using Gases or other Low-flashpoint Fuels	PSV	Pressure Safety Valve
IMO	International Maritime Organization	SSLNG	Small Scale LNG
KPI	Key Performance Indicator	TI	Temperature Index
LNG	Liquefied Natural Gas	VOF	Volume Of Fluid

1. Introduction

In the last decade, the interest in liquefied natural gas (LNG) as a potential alternative energy source with a reduced environmental impact has soared (Speirs et al., 2019). A growing number of projects feature LNG-fueled vehicles coming together with the development of a network of small-scale LNG (SSLNG) storage sites as part of the fuel supply chain (IGU, 2019). Moreover, bulk transport of LNG is expected to grow, due to the extension of the SSLNG network.

However, the spread of LNG technologies poses relevant hazards due to the high flammability of natural gas (Dan et al., 2014; Kalathil et al., 2020; Markowski and Siuta, 2017; Iannaccone et al., 2019). LNG storage areas have a high vulnerability due to the possible occurrence of escalation scenarios and domino effect triggered by fire fires (Casal and Darbra, 2013; Dan et al., 2014; Pitblado and Woodward, 2011). Several scenarios may result in the fire engulfment of LNG tanks: e.g., the ignition of liquid spills following the leak from tank connection pipes, pools of diesel fuel catching fire because of road accidents, etc. The heat released from the fire is transferred through tank walls and an insulating layer to the tank lading (Bubbico and Mazzarotta, 2018; Landucci and Birk, 2013; Scarponi et al., 2018b), leading to the heat-up of the LNG and to pressure build-up. The increment of pressure and the simultaneous weakening of the vessel shell due to the high temperature caused by fire exposure may lead to the catastrophic failure of the exposed equipment, resulting in critical scenarios, such as rapid phase transition (Aursand and Hammer, 2018; Horvat, 2018) or Boiling Liquid Expanding Vapor Explosions (BLEVE) (Abbasi and Abbasi, 2007; Landucci and Birk, 2013). The latter scenario, following the involvement of LNG road tankers exposed to fire following road accidents was documented two times since year 2000 (Planas-Cuchi et al., 2004; Planas et al., 2015).

Therefore, the analysis of the thermal behavior of LNG vessels when exposed to fire is of paramount importance to improve the protection of equipment from industrial fires and to develop safe storage and transport systems. However, a limited number of studies were developed in the technical and scientific literature with the aim of evaluating the thermal response of LNG and, more generally, that of cryogenic vessels exposed to fire scenarios.

Scarponi et al. (2016) set up a non-equilibrium lumped model for the dynamic simulation of pressure build-up and temperature behavior of LNG tanks under fire attack. Despite the model can replicate real accidents

dynamics, taking into account the effect of PSV (pressure safety valve) opening, it considers a single node for the liquid phase. Thus, it is unable to predict liquid temperature stratification. A similar model was developed by Hulsbosch-dam et al. (2017) and was validated using the results of the only experimental study of fire exposure of a cryogenic pressure vessel available to date in the technical and scientific literature. The non-equilibrium model predicts the PSV opening time with good accuracy and can reproduce the experimental results obtained from the bonfire test of a 3 m^3 double-walled tank filled with liquid nitrogen. However, even in this case the model is not able to predict liquid thermal stratification, which is a key parameter for assessing tank pressurization when exposed to severe external heat fluxes. This was documented in several experimental studies dedicated to pressurized tanks exposed to fire (Bradley et al., 2021) and in numerical studies, in which computational fluid dynamics (CFD) approaches were developed for the analysis of LPG (liquefied petroleum gas) tanks exposed to fire engulfing conditions (Scarponi et al., 2018a, 2019) or distance source radiation (Scarponi et al., 2020, 2018b). An extensive review of recent CFD applications in the areas of process safety and loss prevention was carried out by Shen et al. (2020), providing a detailed analysis of studies addressing LNG pool fires and related hazards.

However, the application of advanced numerical studies, such as CFD, to model the thermal behavior of pressurized cryogenic storage tanks exposed to fire heat loads is still lacking.

The aim of this study is to set up an original two-dimensional (2D) numerical approach to describe the behavior of cylindrical, double-walled, pressurized cryogenic storage vessels exposed to high heat loads such as those induced by fire. The prediction of tank internal fluid dynamic is of utmost importance to define the possibility of accident escalation, providing a fundamental understanding of the physical phenomena occurring inside a cryogenic storage tank affected by external fire. The results of this modelling approach can provide valuable information about tank conditions in case of fire that may be helpful to guide emergency response teams as well as to suggest a safe time window for intervention. For this purpose, a set of safety Key Performance Indicators (KPIs) is defined and calculated, based on the results of CFD simulations, thus enabling conservative but realistic considerations on the integrity of LNG tanks exposed to fires.

2. Methodology

2.1. Model description

A range of different technologies for LNG storage is currently available. This study focuses on horizontal double-walled pressure vessels, since these types of tanks represent the preferred technical option for small and medium scale mobility applications and for intermediate storages in the supply chain and distribution network of LNG (Danish Maritime Authority, 2012; Gas Infrastructure Europe, 2020; Lo Brutto, 2019).

A schematic view of the tank geometry and structure is illustrated in Figure 1. A perlite filling and vacuum conditions are present in the annular gap comprised between the inner and outer shell, to provide the required insulation performance (Wartsila, 2018).

A two-dimensional model was developed for the analysis of the response to fire engulfment scenarios of the above-described equipment. The commercial code ANSYS® Fluent® 18.2 was used to perform 2D CFD-based simulations. The governing equations considered are reported in Table 1.

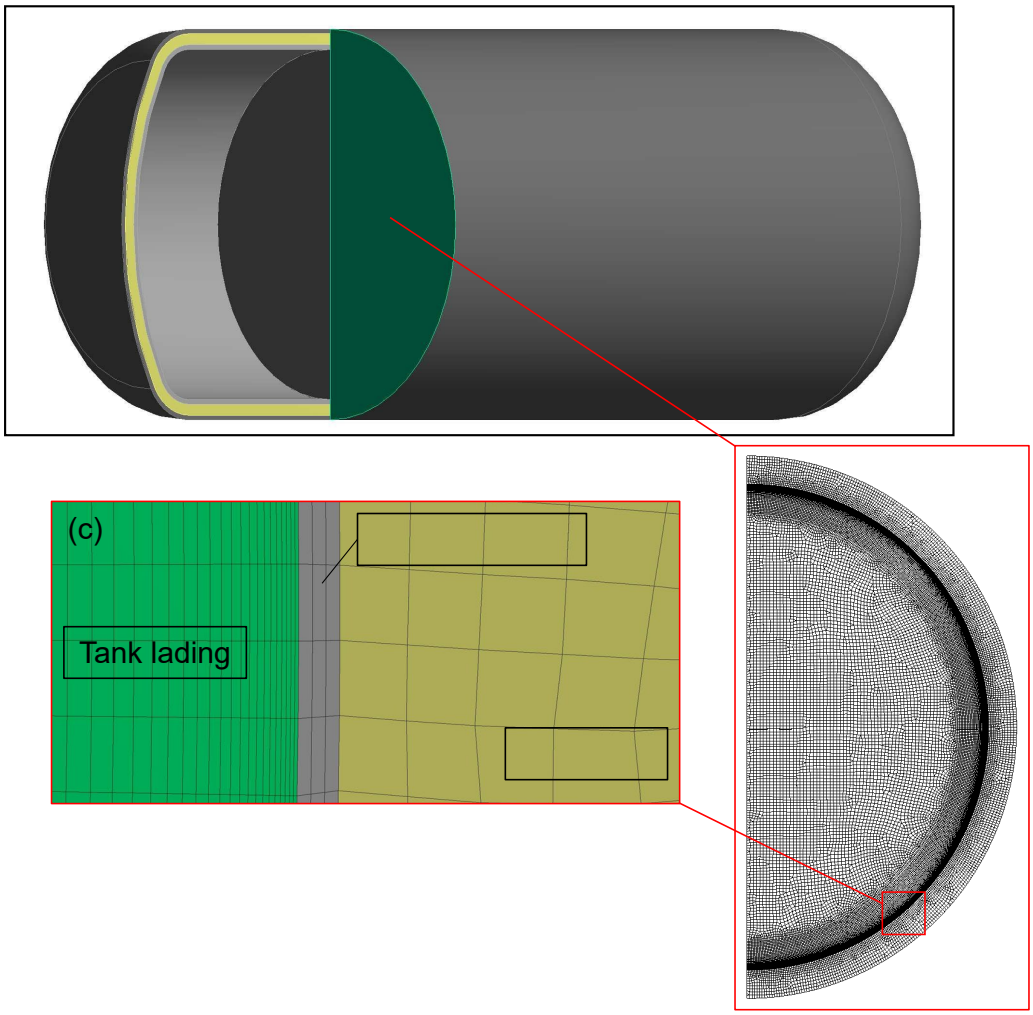

Figure 1: Representation of the computational domain: a) tank section considered for the 2D CFD analysis; b) mesh overview; c) detailed view of the mesh in proximity of the internal wall of the tank, highlighting the different material layers (i.e., insulation, tank inner wall and tank lading).

The continuity equation for the two phases was solved with the Volume Of Fluid (VOF) model (Hirt and Nichols, 1981), adopted in other similar works (Kassemi et al., 2018; Ovidi et al., 2019). The mass transfer between liquid and vapor phases ($m_{L\to V}$ and $m_{V\to L}$) was predicted using the evaporation-condensation model implemented in Fluent, based on the study of Lee (1979) and Knudsen, (1934), considering default evaporation/condensation frequency values (C_{cond} and C_{cond} in Eq. 1 and Eq. 2) as suggested in a previous study by Scarponi et al. (2016).

According to Eq. 1 and Eq. 2, evaporation and condensation take place in a specific domain cell on the basis of temperature, which is calculated at cell pressure. If the temperature is above the calculated saturation temperature (T_{sat}), part of the liquid phase will evaporate, otherwise condensation will occur if temperature is lower than saturation:

$$\dot{m}_{V\to L} = C_{cond}\alpha_V\rho_V\left(\frac{T_{sat}-T}{T_{sat}}\right) \quad \text{Eq. 1}$$

$$\dot{m}_{L\to V} = C_{evap}\alpha_L\rho_L\left(\frac{T-T_{sat}}{T_{sat}}\right) \quad \text{Eq. 2}$$

where α and ρ indicate respectively the volume fraction and density of liquid (L) and vapor (V) phases.

Table 1: Governing equations for turbulent, two phases, transient CFD setup.

Property	**Equations**	**Eq. ID**
Momentum	$\frac{\partial}{\partial t}(\rho \boldsymbol{u}) + \nabla \cdot (\rho \boldsymbol{u}\boldsymbol{u}) = -\nabla \boldsymbol{p} + \rho \boldsymbol{g} + \nabla \cdot \left[\mu \left(\nabla \boldsymbol{u} + (\nabla \boldsymbol{u})^{\mathrm{T}} - \frac{2}{3}\nabla \cdot \boldsymbol{u} I\right)\right] - \nabla \cdot (\rho \boldsymbol{u}' \boldsymbol{u}')$ t: time; ρ: two-phase volume fraction averaged density; $\boldsymbol{p}$: ensemble averaged pressure; $\boldsymbol{u}'$: instantaneous velocity fluctuation; μ: two-phase averaged viscosity; $\boldsymbol{g}$: gravity acceleration; I: identity tensor.	3
Energy (fluid domain)	$\frac{\partial}{\partial t}(\rho E) + \nabla \cdot [\boldsymbol{u}(\rho E + p)] = \nabla \cdot (k_{eff} \nabla T) + \lambda (m_{V \to L} - m_{L \to V})$ E: two-phase ensemble averaged specific energy; k_{eff}: effective thermal conductivity; λ: latent heat of vaporization	4
Energy (solid domain)	$\frac{\partial}{\partial t}(\rho_s Cp_s T_s) = \nabla \cdot (k_s \nabla T_s)$ T_s: solid temperature; k_s: solid thermal conductivity; ρ_s: solid density; Cp_s: solid heat capacity	5
Effective thermal conductivity	$k_{eff} = k + \frac{Cp \mu_T}{Pr_T}$ k: two-phase volume fraction averaged thermal conductivity; Cp: two-phase volume fraction averaged heat capacity; Pr_T: turbulent Prandtl number (=0.85)	6
Turbulent kinetic energy	$\frac{\partial}{\partial t}(\rho K) + \nabla \cdot (\rho K \boldsymbol{u}) = \nabla \cdot \left[\left(\mu + \frac{\mu_T}{\sigma_k}\right) \nabla K\right] + G_K - Y_K$ K: turbulent kinetic energy; μ_T: two-phase volume fraction averaged turbulent viscosity; σ_k: turbulent Prandtl number for K; G_K: generative term for K due to mean velocity gradients; Y_K: dissipative term for K due to turbulence. See (ANSYS Inc., 2018) for definitions of σ_k, G_K and Y_K.	7
Turbulent specific dissipation rate	$\frac{\partial}{\partial t}(\rho \omega) + \nabla \cdot (\rho \omega \boldsymbol{u}) = \nabla \cdot \left[\left(\mu + \frac{\mu_T}{\sigma_\omega}\right) \nabla \omega\right] + G_\omega - Y_\omega$ ω: turbulent specific dissipation rate; σ_ω: turbulent Prandtl number for ω; G_ω: generative term for ω; Y_ω: dissipative term for ω. See (ANSYS Inc., 2018) for definitions of σ_ω, G_ω and Y_ω.	8
Turbulent viscosity	$\mu_T = \alpha^* \frac{\rho k}{\omega}$ See (ANSYS Inc., 2018) for definition of α^*.	9
Secondary phase volume fraction (Liquid)	$\frac{1}{\rho_L}\left[\frac{\partial}{\partial t}(\alpha_L \rho_L) + \nabla \cdot (\alpha_L \rho_L \boldsymbol{u})\right] = m_{V \to L} - m_{L \to V}$ ρ_L: liquid density; α_L: liquid volume fraction; $\boldsymbol{u}$: ensemble averaged velocity; $m_{L \to V}$: evaporation liquid phase source term (see Eq. 1); $m_{V \to L}$: condensation liquid phase source term (see Eq. 2).	10
Primary phase volume fraction (Vapor)	$\alpha_V = 1 - \alpha_L$ α_V: Vapor volume fraction	11
Two-phase averaged material properties	$\psi = \alpha_L \psi_L + (1 - \alpha_L) \psi_V$ ψ: two-phase volume fraction averaged property (where ψ can be density ρ, viscosity μ, turbulent viscosity μ_T or thermal conductivity k. The average value is calculated from liquid and vapor properties (ψ_L and ψ_V, respectively).	12

Based on the estimation of the Rayleigh number of the system ($Ra = g\beta\Delta T\, L^3/\alpha$), the natural convection phenomena occurring inside the tank can be deemed laminar ($Ra < 10^9$) or turbulent ($Ra > 10^9$). The term L can be assumed as the tank internal diameter, β is the thermal expansion coefficient, α the thermal diffusivity, g is the gravity acceleration and ΔT is the temperature difference between tank wall and liquid bulk. For all the case studies described in Section 2.2, the estimated Rayleigh number resulted higher than 10^{10}, hence the free convection boundary layer can be considered turbulent. The *k-ω SST* turbulence model developed by Launder and Spalding (1972) was selected to reproduce the turbulent natural convection regime without the use of wall functions, since the model has been proven valid in previous studies dealing with similar systems (Ovidi et al., 2019; Scarponi et al., 2018a).

To avoid uncertainties related to LNG composition, the model was set up considering tanks filled with pure substances: nitrogen (for the model validation case) and methane (being the main component of LNG mixture) properties were retrieved from NIST database (Lemmon et al., n.d.). Liquid densities, vapor specific heat and thermal conductivity were expressed as function of temperature, whereas all the other fluid properties were kept constant. Vapor phase density was calculated using the Peng-Robinson equation of state (Peng and Robinson, 1976), and stainless steel properties were collected from a NIST cryogenic material properties collection (NIST, n.d.) and relevant EN 10088:2014 (European committee for standardization, 2014).

Thermal properties of the insulation material were calculated according to models proposed by Beikircher and Demharter (2013), who measured the effective thermal conductivity (namely, k_{tot}) of evacuated perlite samples for average temperatures up to 150 °C at mid-section of the specimens and for vacuum pressures ranging from 0.01 to 1000 mbar. Hence, the initial value of k_{tot} was set to 92 mW/(m K), i.e., representative of the experimental vacuum conditions in the annular gap between tank walls. To account for the deterioration of insulation performance, perlite thermal conductivity was increased to a value of 300 mW/(m K), which is conservatively doubled with respect to the maximum value for complete loss of vacuum insulation, based on the study by Beikircher and Demharter (2013). This increased value is intended to be representative of a seriously compromised cryogenic tank insulation, for which vacuum in the annular gap is completely lost and part of the perlite is displaced due to the sudden pressurization.

2.2. Description of the reference simulation cases

The proposed CFD model was validated against data collected from a set of experimental bonfire tests conducted by the Netherlands Organization for Applied Scientific Research (TNO) in 2015 (Kamperveen et al., 2016). The tests were aimed at investigating the possibility of a catastrophic rupture of 3 m^3 cryogenic vessels (storing liquid nitrogen) exposed to radiation intensities higher than 35 kW/m^2, and to understand their thermal and mechanical response in extreme fire exposure conditions.

Table 2: Features of the tanks and initial conditions assumed in the simulation cases considered (MAWP: maximum allowable working pressure; MDT: maximum design temperature; k_{tot}: overall perlite thermal conductivity; ID: tag used in the following to identify the simulation case).

Case ID	Filling degree	Material	Inner diameter [m]	Insulation thickness [m]	Insulation k_{tot} [mW/ (m K)]	Length [m]	Initial pressure [bar]	Initial temperature [°C]	MAWP; MDT [bar;°C]	Nominal capacity [m^3]
	Validation case									
V66	66%	N_2	1.2	0.20	92* / 300**	2.55	2.0	-189.52	7.0; 50	3.0
	Open-deck ship-fuel tank (case-study A)									
A85	85%									
A50	50%	CH_4	4.3	0.25	300**	16.5	6.0	-134.42	11.0; 50	240
A15	15%									
	Road tanker (case-study B)									
B85	85%									
B50	50%	CH_4	2.3	0.12	300**	13.8	1.0	-161.49	3.0; 50	58.0
B15	15%									

*value calculated assuming undamaged insulation
**value calculated assuming damaged insulation

The numerical setup was then used to evaluate the consequences of the exposure to an engulfing fire of larger LNG storage tanks, respectively used for maritime fuel storage and for road LNG transportation. A summary of the tank main features for all the three reference simulation cases is reported in Table 2.

2.2.1. Validation case

The geometry of the 3 m^3 tank and the test conditions were reproduced and implemented in the CFD model. For safety reasons, the experimental campaign was carried out with liquid nitrogen. After the tank filling operation, the cryogenic lading was set to rest for two hours in order to reach stable saturation conditions. Then, propane burners positioned below the tank were ignited, reproducing full engulfment fire conditions. Tank pressure was monitored throughout the fire test and several thermocouples were installed at different positions (e.g., inner and outer tank walls, liquid and vapor ullages).

Unfortunately, temperature measurements during the test resulted in a highly disturbed signal, compromising the reliability of the specific dataset obtained. The external wall temperature reached values over 800 °C on the bottom part, whereas the top section of the tank was heated up to about 600 °C, due to the disturbing effect of wind and the consequent flame tilting. Weakening of the external carbon steel shell eventually resulted in serious structural damages and distortions on the tank shell, leading to the opening of the vacuum rupture disk on the outer wall and causing the displacement of a non-quantified amount of perlite. This resulted in the alteration of the thermal properties of the insulating material, whose thermal conductivity was estimated as indicated in Section 2.1. Further information on the experimental setup and test procedure is reported elsewhere (Hulsbosch-dam et al., 2017; Kamperveen et al., 2016).

2.2.2. Real scale open-deck LNG tank for naval propulsion (Case-study A)

Construction of LNG-fueled vessels shall be compliant to international codes and standards, such as the international maritime organization (IMO) IGF code (IMO, 2015), in which specific requirements are set for the design of gas fuel system and safety features that are to be installed on board. Unlike conventional liquid fuel tanks, which are integrated into the ship structure, the LNG tanks are expected to be independent and they can be installed either within the ship hull or on open deck. In the first case, a gas-tight tank room is required, while the latter arrangement does not need any particular provision.

Most LNG-fueled vessels (other than LNG carriers) are designed to use IMO type C tanks (IMO, 2016). Type C tanks are independent pressure vessels featuring vacuum insulation and double wall structure. Open deck installations have capacities ranging from few hundreds of cubic meters up to 1000 m^3. The annular space enclosed between inner and outer shell contains perlite grains as insulating media, combined with vacuum conditions.

Table 2 reports the features of the 240 m^3 tank considered for the simulation. For sake of comparison, a two-hour full engulfment fire condition was simulated as for the above-described validation case. As reported in the table, a damaged perlite insulation layer was assumed as well, as in the bonfire test, to allow an easier comparison with the validation test results. Different filling degrees of the tank were considered in the simulations, to assess how this parameter affects tank thermal response.

2.2.3. LNG road tanker (Case-study B)

Cryogenic tanks built for road transport application are designed according to prescription given in the ADR regulation (United Nations Economic Commission for Europe (UNECE), 2018) and technical standard EN 13530-2:2002 (European committee for standardization, 2008). The tank concept is similar to type C tanks installed on ships: perlite insulation is kept under vacuum conditions in the annular gap. Table 2 reports the features considered for the 58 m^3 tank. Even in this case, a two-hour full engulfment fire condition was assumed.

2.3. Numerical setup

The solution of the governing equations listed in Table 1 requires the construction of a computational grid. Three unstructured meshes were built in ANSYS® Meshing™, one for each simulation case presented in

Section 2.2. A reduction of required computational time was achieved by imposing a symmetry condition along the transversal axis of the tank (see Figure 1). The adoption of k-ω turbulence model requires a finer grid resolution for the near wall region, that was achieved through the creation of inflation layers starting from the internal wall boundary (see Figure 1c). Further details of the meshes used are reported in Table 3.

The transient nature of the analysis was modelled using a first-order implicit scheme, with a fixed time step of 0.01 s. The under relaxation factors, time step size, and other mesh characteristics were specifically tuned for the proposed model starting from the values adopted in (Scarponi et al. 2018a), as well as the selected discretization schemes reported in Table 3. Grid independence, time step sizes and governing equations convergence criteria were tested for all the simulation results obtained for the validation case (V66, see Table 2), as detailed in Appendix A.

Table 3: Details of numerical setup. Values of under-relaxation factor are reported together with discretization schemes used and main mesh features.

Discretization scheme		***Under relaxation factor***		
Equation/quantity	**Scheme**	**Variable**	**Value**	
Density	2nd order upwind	Pressure	0.3	
Momentum	2nd order upwind	Density	0.7	
Energy	2nd order upwind	Body forces	0.7	
k & ω	2nd order upwind	Momentum	0.5	
Pressure	PRESTO!	Vaporization mass	0.7	
Volume Fraction	Geo-Reconstruction	Turbulent kinetic energy	0.8	
Pressure-velocity coupling	SIMPLEC	Turbulent dissipation rate	0.8	
Gradients		Turbulent viscosity	1.0	
Least square cell-based		Energy	0.8	
Mesh features				
Case ID	**Mesh elements**	**First layer thickness [m]**	**Inflation layers**	**Minimum cell size [m]**
V66	63404	9.9×10^{-5}	45	0.005
A15-A50-A85	30264	7.0×10^{-4}	40	0.030
B15-B50-B85	69533	7.0×10^{-5}	50	0.010

To reproduce the operating conditions of cryogenic storage tanks, the fluid is considered to be at saturated conditions at the initial pressure value, whereas a linear temperature gradient is present between cryogenic lading temperature and ambient temperature (here assumed to be 16 °C for all cases). Fluid is assumed to be initially motionless, hence no velocity field is present. Moreover, turbulent kinetic energy and specific dissipation rate were initialized at 10^{-9} m^2/s^2 and 10^{-3} s^{-1}, respectively. No-slip condition was imposed at the tank inner wall.

Simulation of full-engulfing pool fire scenario was achieved setting a variable heat flux boundary condition at the outer shell wall. The heat flux absorbed by the tank was calculated according to the Stefan-Boltzmann law:

$$\dot{q}'' = \sigma \varepsilon_w (T_f^4 - T_w^4) \qquad \text{Eq. 13}$$

where T_f is the flame blackbody temperature, assumed equal to 860 °C based on experimental measurements (Kamperveen et al., 2016). The subscript *w* refers to wall properties, thus ε_w and T_w are defined as the wall surface emissivity (here conservatively considered equal to 1) and the wall temperature, respectively. This modelling approach has been proven successful in a different range of applications (Landucci et al., 2016; Scarponi et al., 2018) and allows a satisfactory reproduction of actual engulfing fire

boundary conditions, since radiation in hydrocarbon fires may be responsible of up to 80% of the total heat transferred (Birk et al., 2016).

The proposed model, intended for the basic understanding of thermal and fluid dynamics of fire-exposed LNG vessels, does not consider BOG venting or pressure safety valve operation. Rather, it allows modeling a closed system that represents an extreme condition from a safety perspective.

2.4. Safety Key Performance Indicators (KPIs)

Three different KPIs were defined in order to exploit the results obtained from the CFD simulations and to provide an overview of the safety profile of LNG tanks exposed to fire engulfment. The KPIs and their definitions are reported in Table 4. All the KPIs are defined as positive quantities, and values higher than unity indicate potentially unsafe conditions.

Table 4: KPIs defined for the assessment of safety performance of pressurized cryogenic vessels. Specific parameters used in KPI definition are also defined.

KPI symbol	**Equation**	**Definition**	**Eq. ID**
TI	$\frac{S_{max}}{A_{d,C}}$	Quantification of thermal-induced stresses on tank structure	14
PI	$1 - \frac{MAWP - P_t}{MAWP - P_0}$	Quantification of the reduction of design safety margins with respect to stresses induced by internal pressure	15
EI	$\frac{E_{VB}}{E_0}$	Amount of energy released in case of tank failure with respect to a reference value	16
Parameter	**Value/Equation**		**Eq. ID**
$A_{d,C}$	0.48	Critical size of tank insulation defect [m^2] (Scarponi et al., 2017)	-
S_{max}	*	Surface of tank inner wall with a temperature greater than MDT [m^2]	-
$MAWP$	See Table 2	Tank maximum allowable working pressure [bar]	-
P_0	See Table 2	Tank initial pressure [bar]	-
P_t	*	Tank pressure at time t [bar]	-
E_{VB}	$\frac{d\widehat{U}}{\widehat{\Delta H}_{TNT}} \times \eta \times 2$	Energy released in case of vessel burst at ground level, expressed in TNT equivalent mass [kg] (Mannan, 2012)	17
$d\widehat{U}$	*	Variation of tank specific internal energy between initial conditions and the considered time step [kJ/kg]	-
$\widehat{\Delta H}_{TNT}$	4680	TNT specific explosion energy [kJ/kg]	-
η	0.5	Fraction of $d\widehat{U}$ converted into blast wave	-
E_0	0.52	Energy needed to generate a blast wave able to damage pressurized equipment at 5 m distance, expressed in TNT equivalent mass [kg]	-

* Values to be calculated for each time step considered

The first KPI, TI, gives a measure of the thermal stresses to which the internal surface of a fire-exposed double-walled cryogenic tank can be subject. The parameter S_{max} is the extent of the internal surface that is heated by the fire at a temperature higher than the maximum design temperature (MDT). Annex B of European standard EN 13458-2:2002 (European committee for standardization, 2002) states that the MDT for static vacuum insulated austenitic steel vessels is 50 °C (see Table 2). The parameter $A_{d,C}$ is the value of the "critical size" of the overheated surface, that is, the critical extent of the wall surface that, when heated above the MDT, becomes sufficient to jeopardize the integrity of the tank shell (Scarponi et al., 2018). The $A_{d,C}$ value reported in Table 4, which is used for the definition of TI indicator, is based on the experimental results obtained by Birk (2005) and the finite elements modelling carried out by Scarponi et al. (2017). In both studies, the mechanical integrity of LPG tanks with defective thermal protection coating exposed to fire was investigated. Following the definition of TI, the value of the indicator should be 0 under normal operating conditions (absence of a fire) and equals 1 when a portion of the inner wall area as large as $A_{d,C}$ is heated at a temperature higher than the MDT by the external fire.

As expressed by Eq. 15, the indicator PI depends on the dynamic evaluation of the pressure inside the tank, providing a measure for the change in the safety margin with respect to the tank MAWP, which is considered equal to tank design pressure. As for the previous case, the KPI value equals 0 in normal operating conditions. In the presence of an external fire, leading to a pressurization of the tank, the value of the KPI progressively approaches 1, i.e., the limit value at which the internal pressure equals the MAWP. Values above 1 indicate that the internal pressure exceeds MAWP and the possibility of a mechanical failure of the tank.

While TI and PI indicators refer to the inherent safety of the storage tank, EI was defined to provide a quantification of the damage potential following the catastrophic rupture of the vessel that might lead to accident escalation (domino effect) (Tugnoli et al., 2013). Following the vessel burst, the internal energy accumulated inside the tank is suddenly released to the surroundings. A fraction of this energy (the quantity η reported in Table 4) is converted into a blast wave, with a potential damage to the equipment surrounding the LNG tank. A reference minimum energy required to generate a blast wave able to damage the surrounding equipment, E_0, is defined. The value of E_0 is assumed equal to a peak static overpressure of 0.2 bar at 5 m from the explosion center, indicated by Tugnoli et al. (2013) as the reference overpressure threshold to damage pressurized equipment. The damage threshold was derived from equipment-specific models for the calculation of the damage probability developed by Cozzani and Salzano (2004), derived from the collection and analysis of a wide dataset of experimental and observational data. The distance of 5 m was assumed as a lower limit for the distance between adjacent tanks[1].

Thus, as defined by Eq. 16, EI represents the ratio between the explosion energy resulting from vessel burst (E_{VB}) and a reference value for escalation, E_0. Among the different models available in the literature for the estimation of explosion effects, the TNT-equivalence model was used in the present study for the sake of simplicity. Using this model, the explosion energy (thus, both E_0 and E_{VB}) can be expressed as an equivalent amount of TNT, as mentioned in Table 4. Further details about the TNT equivalence model can be found in the literature (Kinney and Graham, 1985; Mannan, 2012). In accordance with the other defined KPIs, a value of EI >1 indicates that blasts following the LNG tank rupture might have the potential for causing a domino effect resulting in accident escalation.

3. Results and discussion

3.1. Model validation

Pressure profiles obtained for two-hour engulfing fire simulations of the 3 m^3 cryogenic vessel are reported in Figure 2 together with the data obtained from the experimental test. A drastic change of the experimental pressurization rate can be observed in the validation test 30 min after the start of fire exposure. The sudden

[1] As required by the European standard EN 1473:2016 (CEN (European committee for standardization), 2016), the separation distance between two LNG tanks must be at least equal to half the diameter of the secondary container of the larger tank. The 5 m limit considered in this study avoids considering a too low and unrealistic equipment spacing.

pressure increase started immediately after the opening of the vacuum rupture disk and the partial release of perlite insulation material, as discussed in Section 2.2.1. Thus, in order to validate the model, simulations were carried out assuming different alternatives for the properties and performances of the insulating layer:

1. Insulated tank, i.e., undamaged tank insulation for the entire duration of the simulation;
2. Damaged insulation since the beginning of the simulation (see below for the description of the assumed damage);
3. Undamaged tank insulation until 30 min after fire is started, then damaged insulation – case V66, see Table 2. The same damage assumed as in simulation 2 was considered;
4. Bare tank (no insulation is present).

All the simulations were run considering the same geometry, initial and boundary conditions of the validation case V66 (see Table 2), thus reproducing the conditions of the experimental test described in Section 2.2.1.

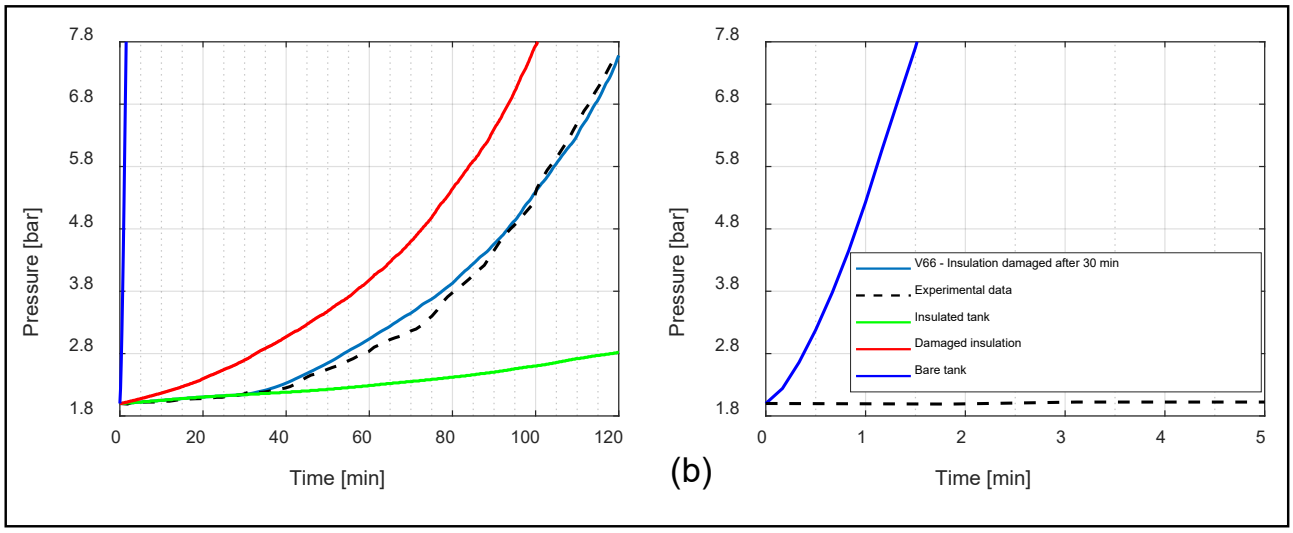

Figure 2: (a) Comparison between experimental and modelled pressurization profiles for the validation case assuming different conditions of the insulation; (b) detail of the pressure build-up obtained for bare tank simulation. V66 simulation case: see Table 2 for details; Insulated tank: no damage is assumed to occur to the insulation; Damaged insulation: insulation assumed damaged since the beginning of the simulation; Bare tank: no insulation considered.

Figure 2 reports the results of the four simulations carried out. Figure 2b shows the extreme and unrealistic situation of a bare LNG tank without thermal insulation. It can be noted that under these conditions the tank will reach the final test pressure level in less than 2 min, following a pressurization transient similar to that experienced for fire-engulfed LPG storage tanks (Scarponi et al., 2018). As shown in Figure 2a, if an undamaged insulating layer is to be considered, the pressurization rate would be well predicted for the first 30 min, but afterwards the model would underestimate the experimental pressure. The thermal conductivity of the undamaged thermal insulation layer was estimated according to the approach described in Section 2.1 (see Table 2).

The worsening of the insulation performance experienced during the bonfire test was likely to be caused by the loss of vacuum in the tank annular gap , together with the displacement of granular perlite. As stated in the experiment report of the validation test (Kamperveen et al., 2016), after 30 min a complete loss of vacuum and partial discharge of perlite occurred in the insulation layer of the tank. To account for this event in the simulation, the properties of the damaged insulation layer were modified (see Table 2 and indications reported in Section 2.1). Simulations showing the performance of such damaged insulation in the validation test are reported in Figure 2a. When the damage is assumed to occur at the beginning of the experimental test, a significant overestimation of the internal pressure build-up is evident. If, as in the experimental report, the damage of the insulation is assumed to occur 30 min after the fire start, the model shows a good agreement

with experimental data: predicted pressure values are comprised in a range between ±3% deviation from measured test data.

As mentioned in Section 2.2.1, unstable temperature measurements were obtained during the validation test. However, as indicated by (Kamperveen et al., 2016), the thermocouples provided stable and reliable values immediately before fire ignition and after fire was stopped. Hence, to obtain at least an indicative representation of the transient heat-up process, a simplified data smoothing was applied, averaging the experimental values obtained from the thermocouples, considering a linear trend among the unbiased values measured at the beginning and at the end of the fire test.

The CFD model performance in reproducing time evolution of liquid and vapor temperatures was assessed following the method proposed by Hanna et al. (1991). This approach requires the calculation of the geometric mean bias (*MG*) and the geometric mean variance (*VG*) of both measured (T_{exp}) and predicted (T_{CFD}) values. Temperatures data from the experimental test and CFD simulation were compared considering 5 min intervals. For each time step (identified by index i), $T_{exp,i}$ and $T_{CFD,i}$ were used to calculate the quantities in Eq. 18 and Eq. 19.

$$MG = exp\left[\overline{\ln(T_{exp})} - \overline{\ln(T_{CFD})}\right] \quad \text{Eq. 18}$$

$$VG = exp\left[\overline{(\ln(T_{exp}) - \ln(T_{CFD}))^2}\right] \quad \text{Eq. 19}$$

Where the terms $\overline{\ln(T_{exp,})}$, $\overline{\ln(T_{CFD,})}$ and $\overline{(\ln(T_{exp}) - \ln(T_{CFD}))^2}$ are calculated in the following way:

$$\overline{\ln(T_{exp,})} = \sum_i \ln(T_{exp,i}) / \sum i \quad \text{Eq. 20}$$

$$\overline{\ln(T_{CFD,})} = \sum_i ln(T_{CFD,i}) / \sum i \quad \text{Eq. 21}$$

$$\overline{(\ln(T_{exp}) - \ln(T_{CFD}))^2} = \sum_i (\ln(T_{exp,i}) - \ln(T_{CFD,i}))^2 / \sum i \quad \text{Eq. 22}$$

The bias in model predictions, i.e., the tendency to systematically over or under-predict temperature values, is expressed by *MG*, whereas the *VG* value is a measure of the scatter in the model predictions around a mean value. Points located to the left of *MG=1* suggest a model over-prediction, whereas points to the right of this value indicate under-prediction. Confidence levels of *MG=0.5* and *MG=2* (representing a factor of two for over and under-prediction respectively) are also reported, defining a range for an "acceptable" model. Note that in Figure 3 a perfect model would be represented by a point at the vertex of the parabola.

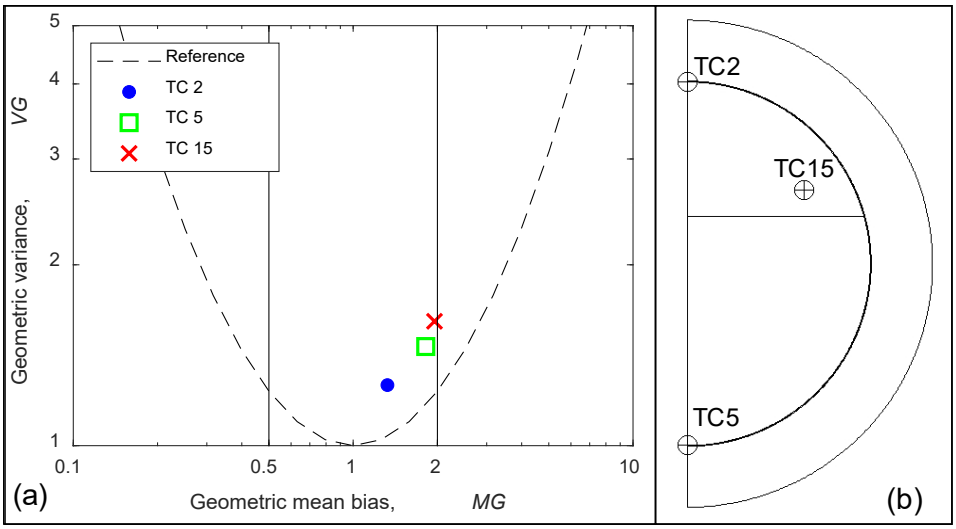

Figure 3: (a) Geometric mean bias (MG) and variance (VG) of model-predicted temperature values compared against experimental measures. (b) Position of liquid-vapor interface and of thermocouples in the experimental bonfire test used for the validation case V66.

As shown in Figure 3, vapor temperature (thermocouple TC 2, located on the top part of vapor ullage) shows a good agreement with experimental data, whereas liquid temperature (TC 5 on the tank bottom) and vapor temperature 8.5 cm above the liquid interface (TC 15) experience more important deviations from test data, even if they remain below the *MG=2* limit.

3.2. Analysis of case studies

Figure 4 shows the pressure rise curve obtained for the other case studies analyzed (see Table 2). Figure 4a shows that in Case-study A, concerning a ship LNG fuel tank, even assuming a degraded thermal insulation layer since the beginning of the simulation, the PSV opening pressure (considered equal to the MAWP value reported in Table 2) is obtained only in the case of very low filling degrees of the tank (15%, see Table 2). The analysis of simulation results clearly indicates that, as expected, higher tank filling degrees result in slower pressurization rates due to the slower heat-up of the tank lading.

After an initial period (approximately the first 10 min of simulation), in which the pressure build-up is limited, the pressurization rate starts to constantly increase, reaching overall average values of about 0.512, 0.337 and 0.271 bar/10 min for cases A15, A50 and A85, respectively. As shown in Figure 4a, the increase in the pressurization rate occurs approximately 20 min after the start of fire exposure.

Similar results were obtained for case-study B, concerning the simulation of an engulfed road tanker. In this case as well, a higher pressure increase is obtained when the filling degree is decreased. However, in this case-study, the exposure to full engulfment conditions results critical for all the three filling degrees analyzed. In simulation case B15, the tank MAWP is reached 30 min before case A15, whereas in cases B50 and B85 this value is reached about half an hour later than case B15. An average pressurization rate of about 0.593 bar/10 min can be estimated in case B15, while cases B50 and B85 have pressurization rates of 0.270 and 0.249 bar/10 min, respectively. Furthermore, comparing Figure 4a and Figure 4b, it is possible to notice that cases B50 and B85 follow an almost identical pressurization trend, differently from what observed for case A, where the filling rate plays a more important role due to the different size of the tank.

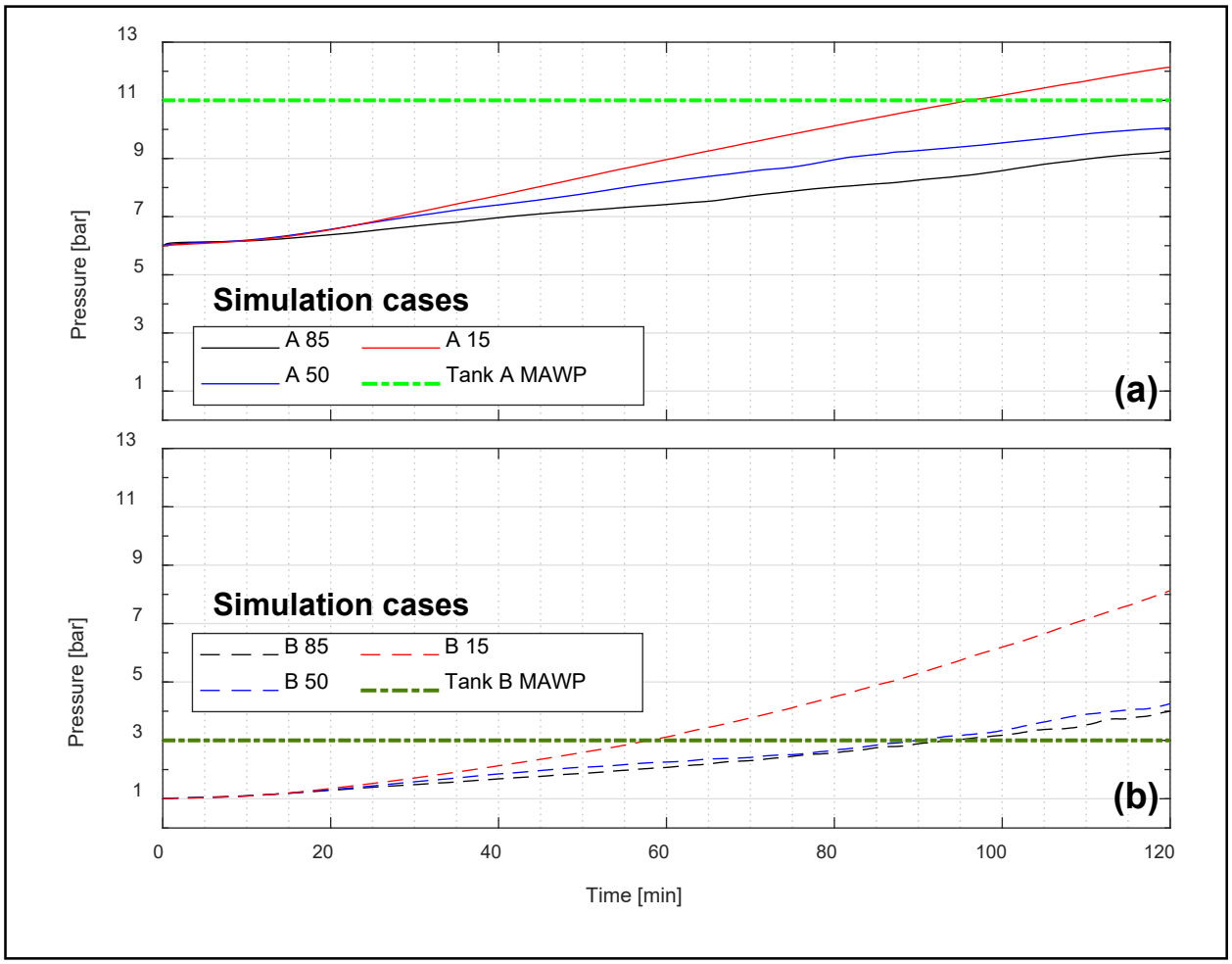

Figure 4: Pressurization profiles for (a) Case-study A (200 m^3 type C tank) and (b) Case-study B (58 m^3 road tanker) engulfed in fire. For the description of simulation cases refer to Table 2.

Besides the pressurization effect related to the thermal expansion of the vapor, pressure rise inside the tank is directly related to the mass of liquid evaporated during fire exposure. Regions of condensation and evaporation inside the tanks are represented in Figure 5. It is possible to notice that for both the simulation cases considered, even after one hour of fire exposure, evaporation takes place only in a very thin region in contact with tank walls (see panels A2 and B2 of Figure 5), whereas the liquid-vapor interface regions farther from the tank walls cool down the vapor, eventually condensing it. As time passes, the size of the evaporation clusters in proximity of the interface and in contact with the tank wall starts to grow. Small residual condensation regions are still present close to the tank bottom: these are zones where the small vapor pockets detaching from bottom walls reach the colder liquid bulk, promptly condensing. Comparing the results obtained for case-studies A and B, it can be noticed that the extension of the evaporating regions at the interface is more limited for case B. This effect might be caused by different initial conditions between the two cases and/or by the different tank sizes. Similar results are obtained for the other cases listed in Table 2, as shown in Appendix B.

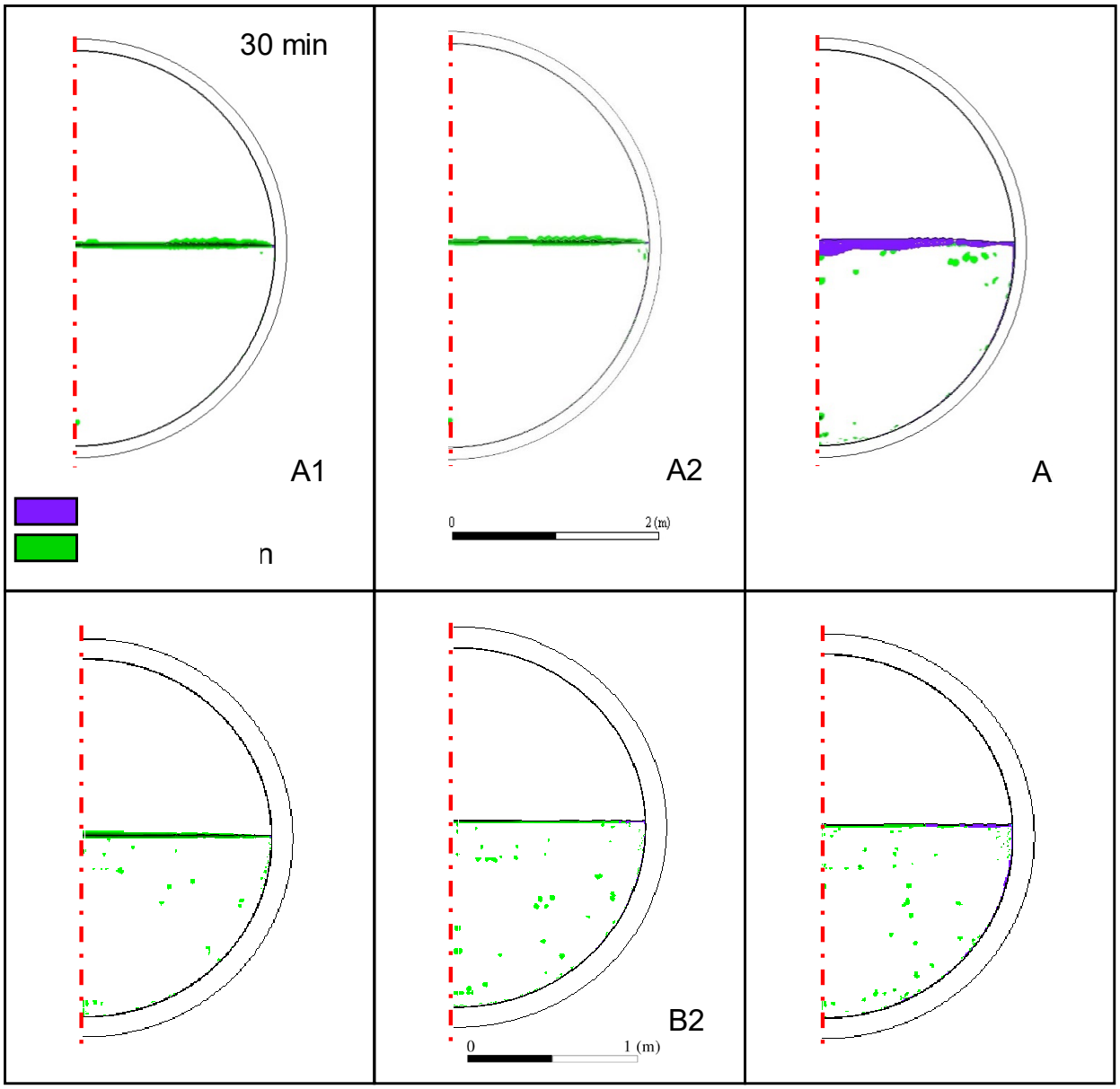

Figure 5: Time evolution of condensation and evaporation regions inside tank lading for simulation cases A50 (panels A1-A3) and B50 (panels B1-B3). Table 2 reports the details of the two simulation cases.

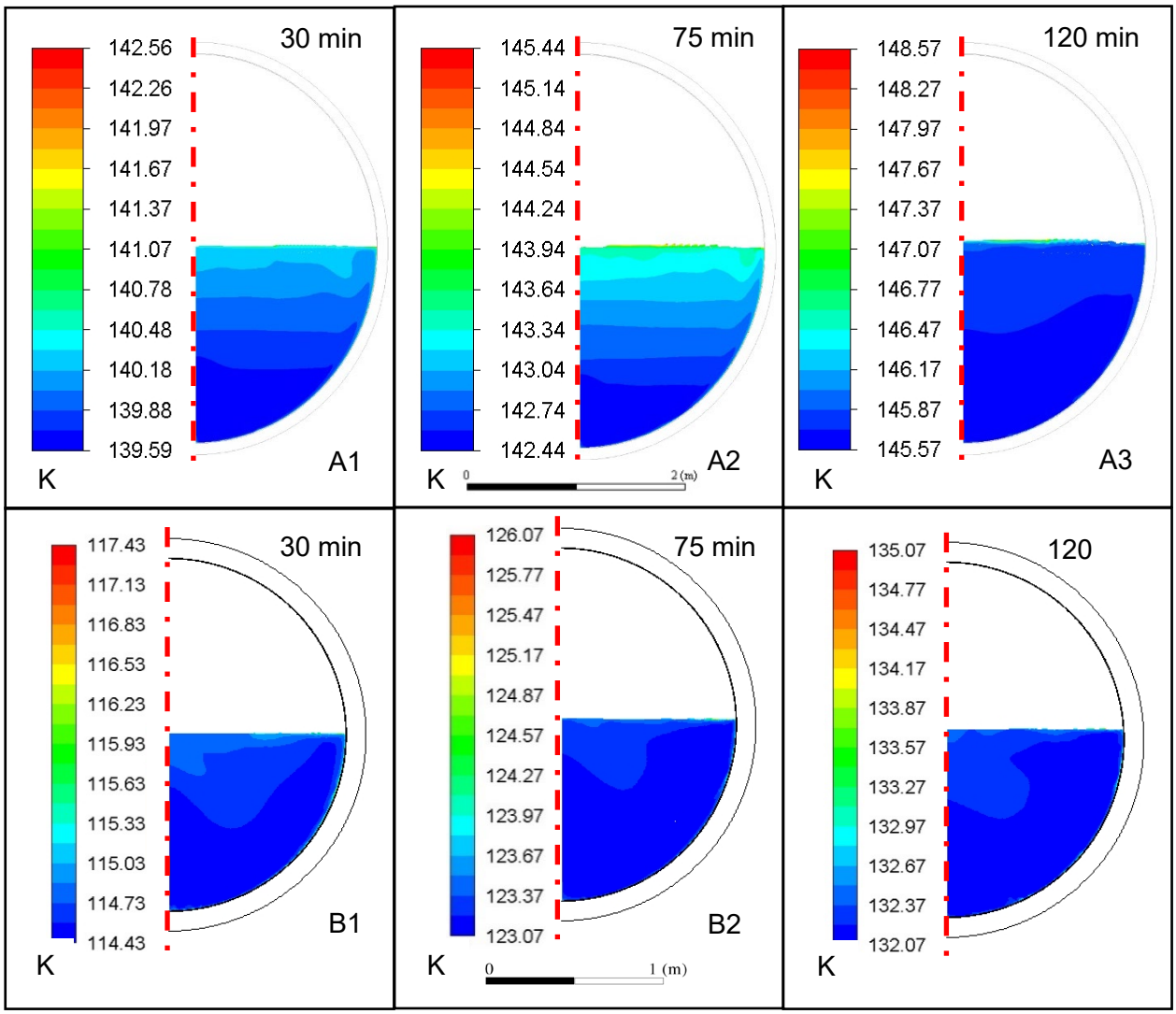

Figure 6: Temperature contour plots (in K) for simulation cases A50 (A1-A3) and B50 (B1-B3) at different times. Table 2 reports the detail of the simulation cases.

Figure 6 shows the liquid temperature distribution at different time steps for case-studies A and B. To better show the evolution of the liquid thermal stratification at the boundary with the vapor/liquid interface, only liquid temperature is reported in the panels. The results obtained for the other cases listed in Table 2 are shown in Appendix B. As clearly shown from the comparison of panels A1 and B1 of Figure 6, after 30 min of fire exposure a slight liquid stratification starts developing on the upper liquid layer for tank A (see panel A1), with temperatures decreasing from 142 to 140.5 K from the vapor/liquid interface up to 1 m depth in the liquid. Conversely, for tank B (see panel B1) a more homogenous situation is predicted, with temperatures differences lower than 1 K from the vapor/liquid interface to the bottom of the tank. This is possibly due to the lower volume and thermal inertia of tank B, inducing a more efficient recirculation and homogenous temperature distribution, as observed for the simulation of LPG tanks (Scarponi et al., 2018a). The same qualitative behavior is also observed for prolonged fire exposure, where again a more pronounced stratification of temperature distribution is observed for tank A (e.g., see the results in panels A2 and A3 with respect to the results in panels B2 and B3 of Figure 6).

Clearly enough, the overall liquid heat-up is more pronounced for tank B than for the case of tank A. Actually, after 120 min of fire exposure, the maximum liquid temperature increment from the initial temperature is of about 23 K for tank B and of 10 K for tank A. Figure 7 shows the dynamic behavior of the maximum wall temperature in the top space of the tank in contact with the vapor phase (i.e., in the position of

TC 2, see Figure 3b). Due to the lower thermal inertia of the vapor phase and to the limited heat transfer coefficients, the temperature growth is more pronounced than in the liquid phase for both tanks, exceeding the MDT after prolonged fire exposure. The influence of the filling degree is more pronounced in the simulations of tank A (see the solid curves in Figure 7), leading to a delayed heat-up of the tank, whose temperature exceeds the MDT after 65 and 80 min of fire exposure for 15 and 85% filling degree values, respectively. Conversely, tank B heat-up is faster than tank A, and MDT is exceeded after only about 45 min in all simulated cases. This evidences a negligible effect of the filling degree and a lower thermal inertia for tank B, both due to the limited volume of the free vapor space that needs to be heated up compared to tank A.

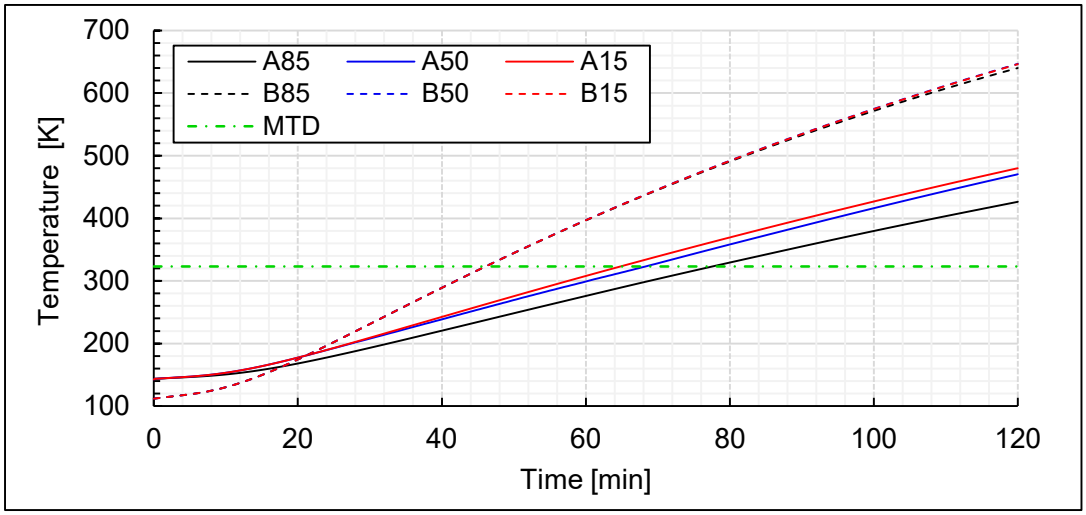

Figure 7: Maximum wall temperature profile calculated for the simulation cases summarized in Table 2.

3.3. KPI values and transition to safety critical regions

The results of 2D CFD simulations were used to evaluate the KPIs defined in Section 2.4, in order to explore the safety margins with respect to regions where the possible structural failure of the selected LNG tanks exposed to fire may occur. Figure 8 reports the values of the KPIs obtained for the different simulation cases after 60, 90 and 120 min since fire ignition. As discussed in Section 2.4, for all the defined KPIs, a value higher than 1 identifies the transition to safety-critical values. Thus, three different volumes were determined in the space defined by the three safety KPIs:

i) a safe region, where all the KPI values considered have values lower than one (green zones in Figure 8);
ii) an intermediate region, in which at least one indicator is higher than one, identifying a potentially dangerous situation (yellow zone in Figure 8);
iii) an unsafe region, in which all the KPI values have values higher than one, exceeding the safety limits (red zone in Figure 8).

Figure 8a reports the values obtained for PI and TI in the different simulation cases. Given the relatively high wall temperatures obtained in the simulations, none of the TI values falls in the safe region except for the case A85 at 60 min of fire exposure. This is due to the combined effect of the high thermal inertia of the liquid lading (i.e., due to the high filling degree) and to the limited time of fire exposure. The results obtained provide a simplified indication of the tank mechanical integrity reduction induced by the thermal weakening. Figure 8a also shows that most of the results are in the yellow region, due to the low PI values obtained associated with the limited pressure build-up (see Figure 4). Only after very long fire exposures, simulation results fall in the red region. This confirms that the risk of tank structural failure is enhanced by a thermal weakening of the steel. The thermal weakening is particularly relevant for tanks having lower filling degrees, due to the higher

extension of the vapor space, in which higher temperature values are obtained. In fact, for the simulation case B15 all KPIs fall inside the red area after 60 min of fire exposure.

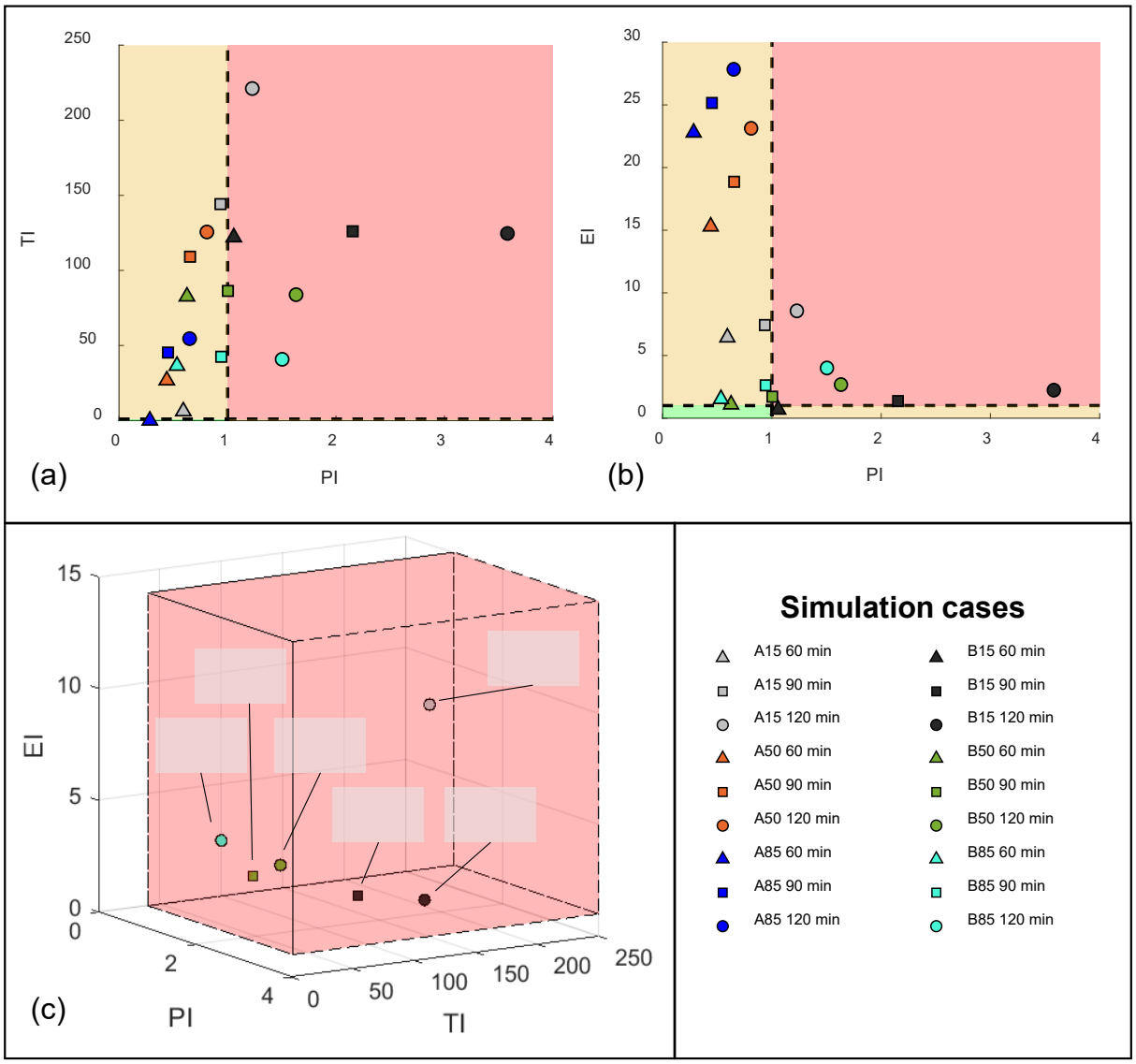

Figure 8: Comparison of safety KPIs for fire-engulfed cryogenic pressure tanks: a) TI (Temperature index) versus PI (Pressure index); b) EI (Energy index) versus PI (Pressure index); c) 3D representation of the unsafe volume where all the three KPIs are above the safety threshold.

Figure 8b shows the values of EI and PI. The results evidence that after 60 min of fire exposure the EI values are always in the unsafe region. This indicates that after 60 min of fire exposure, the energy released by a catastrophic failure of the tank would always be sufficient to cause a domino effect, resulting in an escalation of the accident.

As shown in Figure 8c, six cases were identified having the most critical conditions, since all the three KPIs fall in the unsafe region. Five of these cases are related to case-study B, whilst for the larger tank considered in case-study A, only case A15 falls in the unsafe region after two hours of fire exposure. This indicates that safety-critical scenarios are likely to involve smaller vessels with lower values of LNG inventories. This is due to combined effect of thermal weakening, which affects a higher portion of tank surface in contact with the vapor, and a sufficient energy accumulation, able to lead to relevant escalation effects in case of tank failure, due to the limited thermal inertia of the tank lading. It is evident how a prolonged full-engulfing fire condition (more than 60 min) will undermine tank structural integrity resulting in potential escalating scenarios,

especially for smaller tank dimensions. Thus, a prompt intervention of automated safety systems and of the emergency response team is deemed crucial to avert serious damage to individuals and assets. The application of specific risk based fireproofing strategies in perspective may also be considered, similarly to current practices adopted for the protection of industrial equipment storing flammable materials (Tugnoli et al., 2012).

Therefore, it may be concluded that the results obtained from the case-study evidence how the modelling approach and the KPIs may effectively identify the hazard deriving from specific fire scenarios, identifying conditions where the tank integrity may be compromised. For LNG road tankers in particular, the rapid intervention of emergency responders can result fundamental to avoid the loss of tank physical integrity and the worsening of accident conditions. The results may thus be used to support emergency planning, and more specifically first response actions, allowing the planning of effective response actions minimizing the potential exposure of emergency teams to unsafe conditions.

With respect to design, the results are relevant in particular for LNG storage tanks used for maritime applications. The KPIs defined may constitute a useful tool to increase the safety profile of onshore LNG storage facilities adopting type C tanks and falling under the obligations of accident prevention policies, such as the Seveso III directive in Europe (European Commission, 2012). Based on the analysis of the potential fire scenarios and of the related KPI values, different safety measures might be considered for installation, depending on the position of the tank (above or below deck), such as the inerting of ship compartment where tanks are installed or the increase of separation distances between adjacent equipment.

4. Conclusions

The aim of the present study was the investigation of the thermal response of LNG tanks engulfed in fires. A 2D CFD model was developed, validated, and extended to large-scale tanks of industrial interest, simulating fire engulfment scenarios. The results provide insights on the evolution of pressure and temperature during fire exposure, along with the distribution of evaporation regions during fire engulfment of insulated tanks. The results evidence that the pressurization rate is higher with lower liquid levels. Extended fire exposure is necessary to reach critical values of pressure build-up in the vessels. The results obtained highlight the influence of thermodynamic and geometrical features over the spatial distribution of evaporating zones and temperature fields inside cryogenic tanks, and the importance to further investigate such phenomena, in order to accurately predict the evaporation rate, causing tank pressurization, resulting from fire exposure.

The set of defined KPIs was suitable to identify the possible transition to safety-critical regions of the tanks exposed to fire, where structural integrity may be affected and a high potential for domino effects resulting in accident escalation is present. The values obtained for the KPIs in the simulation cases highlighted the relationship between the hazards originating from pressure build-up and thermal weakening of the tank structure. Moreover, despite higher filling degrees result in a higher escalation potential, critical safety conditions are reached more rapidly for cases having a lower liquid level and a lower inventory.

The KPIs defined thus allow for the identification of critical trends and unsafe conditions during fire exposure of LNG tanks, providing a useful support for the design of safety systems and for the planning of emergency response The set of KPIs defined was suitable to identify the possible transition of the tanks exposed to fire to safety-critical regions, where structural integrity may be affected and a high potential for domino effects resulting in accident escalation is present. The values obtained for the KPIs in the simulation cases highlighted the relationship between the hazards originating from pressure-build up and thermal weakening of the tank structure. Moreover, despite higher filling degrees results in a higher escalation potential, critical safety conditions are reached more rapidly for cases having a lower liquid level and a lower inventory. The KPIs defined thus allow for the identification of critical trends and unsafe conditions during fire exposure of LNG tanks, providing a useful support for the design of safety systems and for the planning of emergency response. The modelling approach and the KPIs allow identifying the scenarios that may lead to

unsafe conditions for the tank, supporting the planning of effective first response actions accounting for the safety of responders.

References

Abbasi, T., Abbasi, S.A., 2007. The boiling liquid expanding vapour explosion (BLEVE): Mechanism, consequence assessment, management. J. Hazard. Mater. 141, 489–519. https://doi.org/10.1016/J.JHAZMAT.2006.09.056

ANSYS Inc., 2018. ANSYS Fluent User Guide, Release 18.2.

Aursand, E., Hammer, M., 2018. Predicting triggering and consequence of delayed LNG RPT. J. Loss Prev. Process Ind. 55, 124–133. https://doi.org/10.1016/j.jlp.2018.06.001

Beikircher, T., Demharter, M., 2013. Heat Transport in Evacuated Perlite Powders for Super-Insulated Long-Term Storages up to 300 °C. J. Heat Transfer 135, 051301. https://doi.org/10.1115/1.4023351

Birk, A.M., Otremba, F., Gonzalez, F., Prabhakaran, A., Borch, J., Bradley, I., Bisby, L., 2016. Fire Testing of Total Containment Pressure Vessels. Chem. Eng. Trans. 48. https://doi.org/10.3303/CET1648047

Birk, A.M., 2005. Tank-car thermal protection defect assessment: Updated thermal modelling with results of fire testing. Montreal, Quebec H3A 2R3, Canada.

Bradley, I., Scarponi, G.E., Otremba, F., Birk, A.M., 2021. An overview of test standards and regulations relevant to the fire testing of pressure vessels. Process Saf. Environ. Prot. 145, 150–156. https://doi.org/10.1016/j.psep.2020.07.047

Bubbico, R., Mazzarotta, B., 2018. Dynamic response of a tank containing liquefied gas under pressure exposed to a fire: A simplified model. Process Saf. Environ. Prot. 113, 242–254. https://doi.org/10.1016/j.psep.2017.10.016

Casal, J., Darbra, R.-M., 2013. Analysis of Past Accidents and Relevant Case-Histories. Domino Eff. Process Ind. 12–29. https://doi.org/10.1016/B978-0-444-54323-3.00002-6

CEN (European committee for standardization), 2016. EN 1473:2016: Installation and equipment for liquefied natural gas - Design of onshore installations. CEN, Brussels, Belgium.

Cozzani, V., Salzano, E., 2004. The quantitative assessment of domino effects caused by overpressure: Part I. Probit models. J. Hazard. Mater. 107, 67–80. https://doi.org/10.1016/j.jhazmat.2003.09.013

Dan, S., Lee, C.J., Park, J., Shin, D., Yoon, E.S., 2014. Quantitative risk analysis of fire and explosion on the top-side LNG-liquefaction process of LNG-FPSO. Process Saf. Environ. Prot. 92, 430–441. https://doi.org/10.1016/j.psep.2014.04.011

Danish Maritime Authority, 2012. North European LNG Infrastructure Project - A feasibility study for an LNG filling station infrastructure and test of recommendations. Copenhagen, Denmark.

European Commission, 2012. European Parliament and Council Directive 2012/18/EU of 4 July 2012 on control of major-accident hazards involving dangerous substances, amending and subsequently repealing council directive 96/82/EC. Off. J. Eur. Communities L197, 1–37.

European committee for standardization, 2014. Stainless steels Part 1 : List of stainless steels. CEN, Brussels, Belgium.

European committee for standardization, 2008. Cryogenic vessels - Large transportable vacuum insulated vessels - Part 1: Fundamental requirements. CEN, Brussels, Belgium.

European committee for standardization, 2002. Cryogenic vessels - Static vacuum insulated vessels - Part 2: Design, fabrication, inspection and testing. CEN, Brussels, Belgium.

Gas Infrastructure Europe, 2020. GIE Small Scale LNG Map [WWW Document]. URL https://www.gie.eu/index.php/gie-publications/databases/lng-database (accessed 7.3.20).

Hanna, S.R., Strimaitis, D.G., Chang, J.C., 1991. Hazard response modeling uncertainty (a quantitative method).

Hirt, C.., Nichols, B.., 1981. Volume of fluid (VOF) method for the dynamics of free boundaries. J. Comput. Phys. 39, 201–225. https://doi.org/10.1016/0021-9991(81)90145-5

Horvat, A., 2018. CFD methodology for simulation of LNG spills and rapid phase transition (RPT). Process Saf. Environ. Prot. 120, 358–369. https://doi.org/10.1016/j.psep.2018.09.025

Hulsbosch-dam, C., Atli-veltin, B., Kamperveen, J., Velthuis, H., Reinders, J., Spruijt, M., 2017. Thermodynamic aspects of an LNG tank in fire and experimental validation. EPJ Web Conf. 143, 0–5. https://doi.org/10.1051/epjconf/201714302039

Iannaccone, T., Landucci, G., Scarponi, G.E., Bonvicini, S., Cozzani, V., 2019. Inherent safety assessment of alternative technologies for LNG ships bunkering. Ocean Eng. 185, 100–114. https://doi.org/10.1016/j.oceaneng.2019.05.028

IGU, 2019. 2019 World LNG Report. Barcelona, Spain.

IMO, 2016. Studies on the feasibility and use of lng as a fuel for shipping. Air Pollut. energy Effic. Stud.

International Maritime Organization (IMO), 2015. International code of safety for ships using gases or other low-flashpoint fuels (IGF CODE).

Kalathil, M.J., Renjith, V.R., Augustine, N.R., 2020. Failure mode effect and criticality analysis using dempster shafer theory and its comparison with fuzzy failure mode effect and criticality analysis: A case study applied to LNG storage facility. Process Saf. Environ. Prot. 138, 337–348. https://doi.org/10.1016/j.psep.2020.03.042

Kamperveen, J.P., Spruijt, M.P.N., Reinders, J.E.A., 2016. Heat load resistance of cryogenic storage tanks – Results of LNG Safety Program. Utrecht, The Netherlands.

Kassemi, M., Kartuzova, O., Hylton, S., 2018. Validation of two-phase CFD models for propellant tank self-pressurization: Crossing fluid types, scales, and gravity levels. Cryogenics (Guildf). 89, 1–15. https://doi.org/10.1016/J.CRYOGENICS.2017.10.019

Kinney, G.F., Graham, K.J., 1985. Explosive Shocks in Air, Explosive Shocks in Air. Springer Berlin Heidelberg. https://doi.org/10.1007/978-3-642-86682-1

Knudsen, M., 1934. The Kinetic Theory of Gases: Some Modern Aspects.

Landucci, G., Birk, M., 2013. Heat Radiation Effects, in: Domino Effects in the Process Industries. pp. 70–115. https://doi.org/10.1016/B978-0-444-54323-3.00005-1

Landucci, G., D'Aulisa, A., Tugnoli, A., Cozzani, V., Birk, A.M., 2016. Modeling heat transfer and pressure build-up in LPG vessels exposed to fires. Int. J. Therm. Sci. 104, 228–244.

Launder, B.E., Spalding, D.B., 1972. Lectures in Mathematical Models of Turbulence. Academic Press, London, England.

Lee, W.H., 1979. A pressure iteration scheme for two-phase modeling. Los Alamos Sci. Lab. Los Alamos, New Mex. Tech. Rep. LA-UR 79–975.

Lemmon, E.W., McLinden, M.O., Friend, D.G., n.d. Thermophysical Properties of Fluid Systems, in: Linstrom, P.J., Mallard, W.G. (Eds.), NIST Chemistry WebBook, NIST Standard Reference Database Number 69. National Institute of Standards and Technology, Gaithersburg MD, USA. https://doi.org/https://doi.org/10.18434/T4D303

Lo Brutto, F.M., 2019. Opportunities and constraints for a small-scale LNG development in the Mediterranean sea: Exploit experiences to apply locally, in: Offshore Mediterranean Conference and Exhibition 2019, OMC 2019. Ravenna, Italy, pp. 1–13.

Mannan, S. (Ed.), 2012. Explosion, in: Lees' Loss Prevention in the Process Industries. Butterworth-Heinemann, pp. 1367–1678. https://doi.org/10.1016/b978-0-12-397189-0.00017-3

Markowski, A.S., Siuta, D., 2017. Selection of representative accident scenarios for major industrial accidents. Process Saf. Environ. Prot. 111, 652–662. https://doi.org/10.1016/j.psep.2017.08.026

NIST, n.d. Material Properties: 304 Stainless (UNS S30400) [WWW Document]. URL https://trc.nist.gov/cryogenics/materials/304Stainless/304Stainless_rev.htm (accessed 6.3.19).

Ovidi, F., Pagni, E., Landucci, G., Galletti, C., 2019. Numerical study of pressure build-up in vertical tanks for cryogenic flammables storage. Appl. Therm. Eng. 161, 114079. https://doi.org/10.1016/j.applthermaleng.2019.114079

Peng, D.-Y., Robinson, D.B., 1976. A New Two-Constant Equation of State. Ind. Eng. Chem. Fundam. 15, 59–64. https://doi.org/10.1021/i160057a011

Pitblado, R.M., Woodward, J.L., 2011. Highlights of LNG risk technology. J. Loss Prev. Process Ind. 24, 827–836. https://doi.org/10.1016/j.jlp.2011.06.009

Planas-Cuchi, E., Gasulla, N., Ventosa, A., Casal, J., 2004. Explosion of a road tanker containing liquified natural gas. J. Loss Prev. Process Ind. 17, 315–321. https://doi.org/10.1016/j.jlp.2004.05.005

Planas, E., Pastor, E., Casal, J., Bonilla, J.M., 2015. Analysis of the boiling liquid expanding vapor explosion (BLEVE) of a liquefied natural gas road tanker: The Zarzalico accident. J. Loss Prev. Process Ind. 34, 127–138. https://doi.org/10.1016/j.jlp.2015.01.026

Scarponi, G.E., Landucci, G., Birk, A.M., Cozzani, V., 2018a. LPG vessels exposed to fire: Scale effects on pressure build-up. J. Loss Prev. Process Ind. 56, 342–358. https://doi.org/10.1016/J.JLP.2018.09.015

Scarponi, G.E., Landucci, G., Heymes, F., Cozzani, V., 2018b. Experimental and numerical study of the behavior of LPG tanks exposed to wildland fires. Process Saf. Environ. Prot. 114, 251–270. https://doi.org/10.1016/J.PSEP.2017.12.013

Scarponi, G.E., Landucci, G., Ovidi, F., Cozzani, V., 2016. Lumped model for the assessment of the thermal and mechanical response of LNG tanks exposed to fire. Chem. Eng. Trans. 53, 307–312. https://doi.org/10.3303/CET1653052

Scarponi, G.E., Landucci, G., Tugnoli, A., Cozzani, V., Birk, A.M., 2017. Performance assessment of thermal protection coatings of hazardous material tankers in the presence of defects. Process Saf. Environ. Prot. 105, 393–409. https://doi.org/10.1016/J.PSEP.2016.10.009

Scarponi, G.E., Landucci, G., Birk, A.M., Cozzani, V., 2019. An innovative three-dimensional approach for the simulation of pressure vessels exposed to fire. J. Loss Prev. Process Ind. 61, 160–173. https://doi.org/10.1016/j.jlp.2019.06.008

Scarponi, G.E., Pastor, E., Planas, E., Cozzani, V., 2020. Analysis of the impact of wildland-urban-interface fires on LPG domestic tanks. Saf. Sci. 124, 104588. https://doi.org/10.1016/j.ssci.2019.104588

Shen, R., Jiao, Z., Parker, T., Sun, Y., Wang, Q., 2020. Recent application of Computational Fluid Dynamics (CFD) in process safety and loss prevention: A review. J. Loss Prev. Process Ind. https://doi.org/10.1016/j.jlp.2020.104252

Speirs, J., Balcombe, P., Blomerus, P., Stettler, M., Brandon, N., Hawkes, A., 2019. Can natural gas reduce emissions from transport? Heavy goods vehicles and shipping. London, UK.

Tugnoli, A., Cozzani, V., Di Padova, A., Barbaresi, T., Tallone, F., 2012. Mitigation of fire damage and escalation by fireproofing: A risk-based strategy. Rel.Eng.Syst.Saf. 105, 25–35. https://doi.org/10.1016/j.ress.2011.11.002

Tugnoli, A., Bonvicini, S., Salzano, E., 2013. 9 – Threshold-Based Approach, in: Domino Effects in the Process Industries. pp. 189–207. https://doi.org/10.1016/B978-0-444-54323-3.00009-9

United Nations Economic Commission for Europe (UNECE), 2018. European Agreement concerning the international carriage of dangerous goods by road. New York and Geneva.

Wartsila, 2018. Small- and medium-scale LNG terminals 16.

Appendix A. Grid and time step independence study

This appendix presents the main results of the grid and time-step independence study, all referring to the simulation of the validation case (V66, see Table 2). The finer mesh used for the grid independence study was created reducing the maximum element size and length, whereas the dimension of the first cell close to tank's inner wall was held constant. This resulted in a mesh having around 2.3 times the number of elements reported in Table 3. To investigate the effects of time step size on modelling results, a transient simulation with a doubled time step size, namely 0.02 s, was run. To prove that modelling results are independent from the selected convergence criteria, an additional simulation was run with more stringent criteria. The sum of scaled residual for continuity, momentum and energy equations was required to be one order of magnitude lower than previous setting (from 10^{-3} to 10^{-4} for continuity and momentum; 10^{-6} to 10^{-7} for energy equation). The results of the model independence study are reported in Figure A1, in which the variation of pressure predictions from the model setup used for independence testing are plotted against the results of the benchmark model used for the validation case (V66, see Table 2). It is possible to notice that the differences between the results of the two models are always lower than 3%, thus confirming the robustness and stability of the numerical setup adopted.

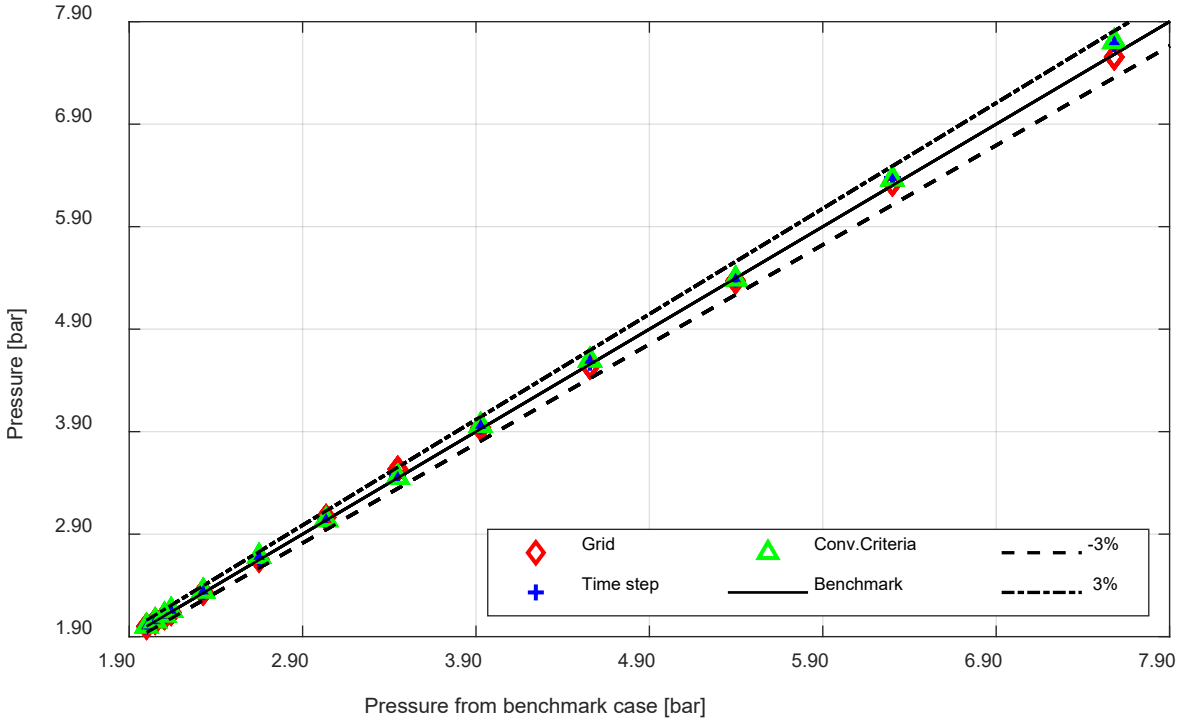

Figure A1: Parity plot reporting the results of the grid independence analysis.

Appendix B. Additional results for the case studies

B.1 Additional results for cases A85 and B85

The results reported in this appendix are analogous to those presented in Section 3.2 for the cases A50 and B50. The extent of evaporation and condensation clusters inside the tank lading are shown in Figure B.1 for three reference time steps (panels A1-A3 for case A85 and B1-B3 for case B85).

It can be noticed that evaporation regions appear to be smaller than those highlighted in Figure 5 for both case A85 and B85. These results may be linked to the slower pressurization rate of storage tanks with a higher filling degree, as seen in Figure 4. A reduction of condensation zones in the bulk region of case B85 (panel B2) can be observed compared to analogous results of case B50.

The dynamic evolution of the temperature inside the tank is illustrated in panels A1-A3 and B1-B3 of Figure B.2. For case A85, temperature values and trend similar to those obtained for case A50 are predicted. Instead, for case B85, the temperature stratification becomes more pronounced than in case B50; this is particularly evident from the observation of panels B3 of Figure B.2 and Figure 6, respectively for case B85 and B50 (obtained after 120 min of simulation). This is possibly due to the larger liquid inventory associated with the incremented filling degree of case B85, obtaining a similar behavior to the one of the larger tank A.

B.2 Additional results for cases A15 and B15

The evaporation and condensation regions inside the tank lading are depicted in Figure B.1 for three time steps of reference (panels A4-A6 and B4-B6).

Compared to the situation reported in Figure 5, the extent of evaporation zones for lower filling degrees is much higher and an evaporation cluster can be found in proximity of tank wall, close to the interface, already after 30 min of fire exposure. Process conditions of case B15 seem to be more favorable for the evaporation process than those encountered in case A15. The greater extension of evaporating regions for lower liquid levels can be correlated to the faster pressurization dynamic observed for these cases.

The dynamic evolution of the temperature in the liquid phase is illustrated in Figure B.2 (panels A4-A6 for case A15 and B4-B6 for case B15). Compared to the temperature profiles observed for cases A50 and B50 (see Figure 6), both cases A15 and B15 feature a more homogenous liquid temperature profile. In other words, the stratification is poorly observed in cases at 15% filling degree, for which also higher temperature increments are predicted compared to the cases at 50% filling degree. In fact, the temperature increase is about 17 and 36 K from the initial temperature, thus almost doubled compared to the simulations at higher filling degrees. This is possibly due to the limited thermal inertia of the liquid phase, which induces larger recirculation and consequent energy accumulation in the tank lading.

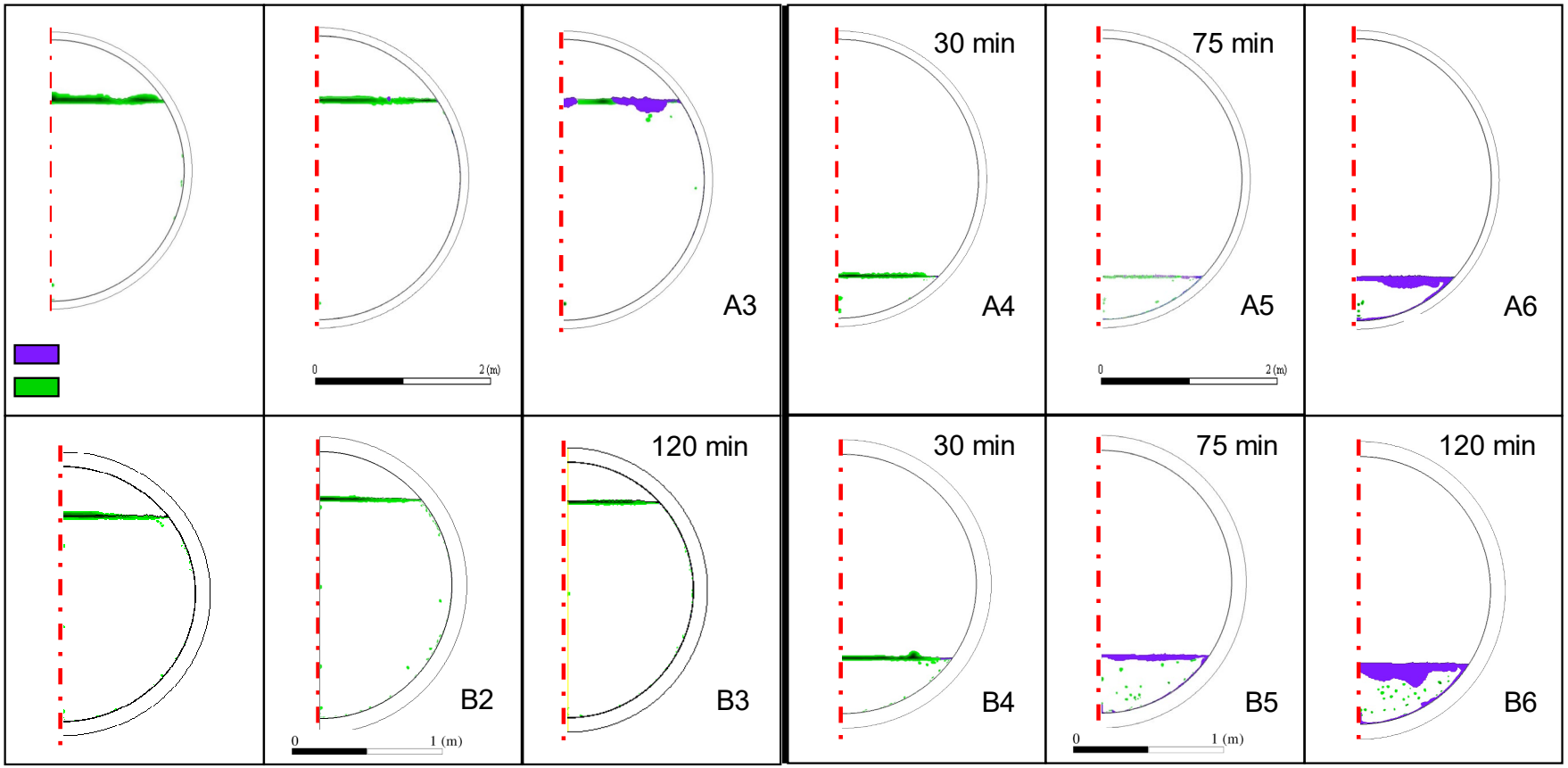

Figure B.1: Time evolution of condensation and evaporation regions inside tank lading for cases A85 (A1-A3); B85 (B1-B3); A15 (A4-A6) and B15 (B4-B6).

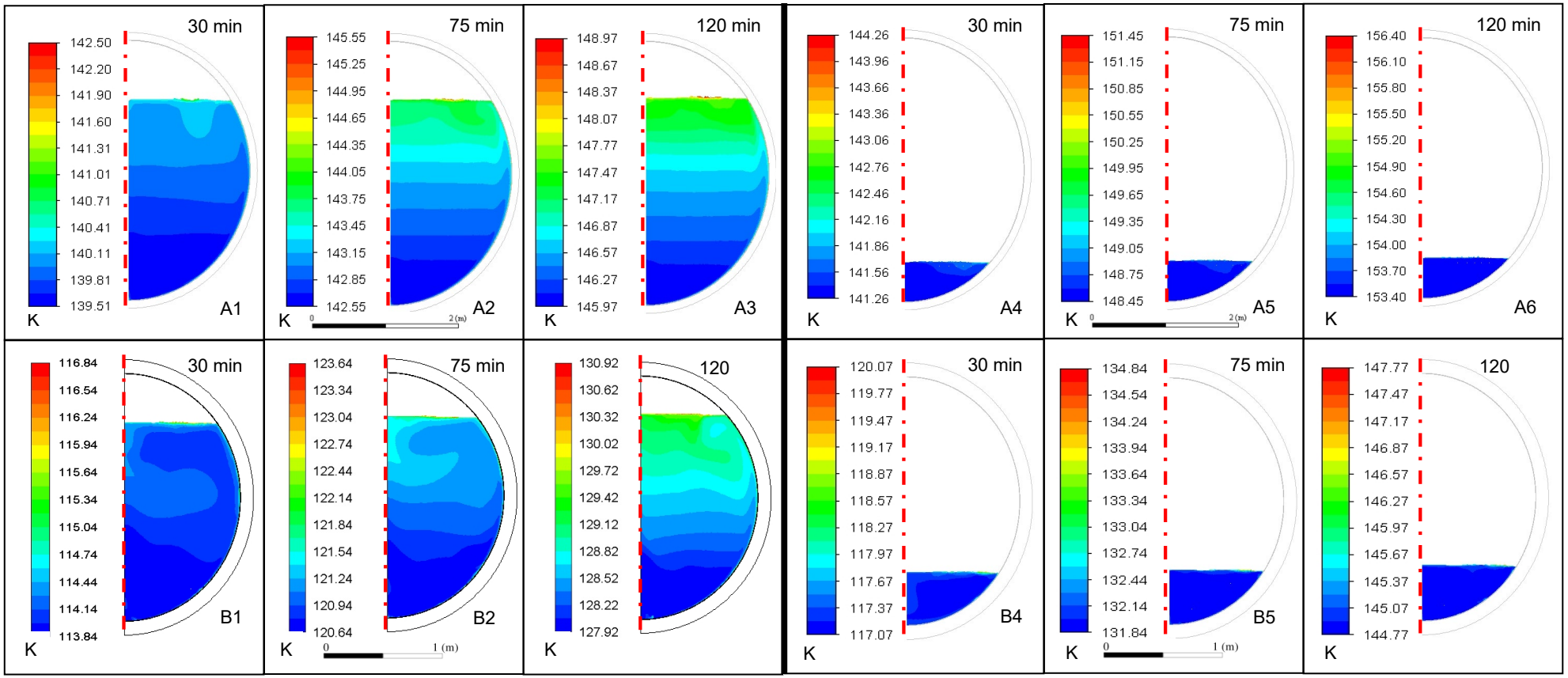

Figure B.2: Temperature contour plots (in K) for cases A85 (A1-A3); B85 (B1-B3); A15 (A4-A6) and B15 (B4-B6) at different times.